

NaviAirway: a Bronchiole-sensitive Deep Learning-based Airway Segmentation Pipeline

Andong Wang, Terence Chi Chun Tam, Ho Ming Poon, Kun-Chang Yu, and Wei-Ning Lee

Abstract—Airway segmentation is essential for chest CT image analysis. Different from natural image segmentation, which pursues high pixel-wise accuracy, airway segmentation focuses on topology. The task is challenging not only because of its complex tree-like structure but also the severe pixel imbalance among airway branches of different generations. To tackle the problems, we present a *NaviAirway* method which consists of a bronchiole-sensitive loss function for airway topology preservation and an iterative training strategy for accurate model learning across different airway generations. To supplement the features of airway branches learned by the model, we distill the knowledge from numerous unlabeled chest CT images in a teacher-student manner. Experimental results show that *NaviAirway* outperforms existing methods, particularly in the identification of higher-generation bronchioles and robustness to new CT scans. Moreover, *NaviAirway* is general enough to be combined with different backbone models to significantly improve their performance. *NaviAirway* can generate an airway roadmap for Navigation Bronchoscopy and can also be applied to other scenarios when segmenting fine and long tubular structures in biomedical images. The code is publicly available on <https://github.com/AntonotnaWang/NaviAirway>.

Index Terms—Airway segmentation, Computed Tomography (CT), Tree-like Structures, Topology, Training Strategy

I. INTRODUCTION

COMPUTED Tomography (CT) [1] prevails in the assessment of lung diseases, such as lung cancer and chronic obstructive pulmonary disease (COPD). Airway segmentation plays a vital role in the CT image analysis procedure. For example, Navigation Bronchoscopy (NB) is the safest and superior for accessing peripheral pulmonary lesions [2]. For better procedural efficiency and patient care, NB requires a pre-planned 3D airway road map that is segmented and reconstructed from CT images. The road map navigates the

This project was in part supported by COVID-19 Action Seed Funding of Faculty of Engineering, The University of Hong Kong. Wei-Ning Lee is the corresponding author.

Andong Wang is with the Department of Electrical and Electronic Engineering, The University of Hong Kong, Hong Kong, China (e-mail: wangad@connect.hku.hk).

Terence Chi Chun Tam is with Respiratory Division, Department of Medicine, The University of Hong Kong, Hong Kong, China, and also with Queen Mary Hospital, Hong Kong, China (e-mail: tcctam@netvigator.com).

Ho Ming Poon is with the Department of Electrical and Electronic Engineering, The University of Hong Kong, Hong Kong, China (e-mail: hmpoon6@connect.hku.hk).

Kun-Chang Yu is with Broncus Medical, Inc., San Jose, CA, 95134 USA (e-mail: jyu@broncus.com).

Wei-Ning Lee is with the Department of Electrical and Electronic Engineering, The University of Hong Kong, Hong Kong, China, and also with the Biomedical Engineering Programme, The University of Hong Kong, Hong Kong, China (e-mail: wnlee@eee.hku.hk).

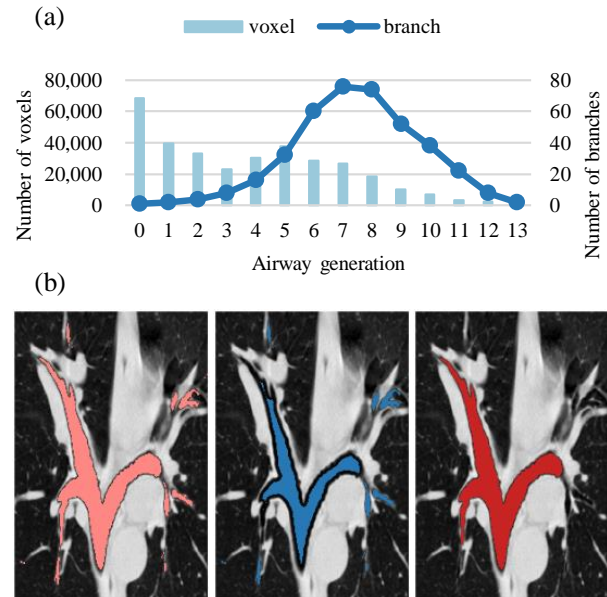


Fig. 1. (a) Bar chart: Low-generation airways take up most voxels but have very few branches. (b) The CT image comes from Binary Airway Segmentation (BAS) dataset [8]. From left to right: reference label; the segmentation which has lower dice accuracy but preserves topology; the segmentation which has higher dice accuracy but loses substantial topological information. Our *NaviAirway* tackles the size imbalance problem while achieving high topological accuracy.

bronchoscope down into bronchioles for target nodule sampling [3]–[5]. In the case of COPD, airway segmentation from CT images is the key to accurate measurement of the lumen size and wall thickness of each target airway [6].

Airway segmentation is different from natural image segmentation as voxel-wise accuracy is no longer the main concern. Instead, a topologically accurate segment (i.e., preservation of branch connectedness and detection of fine bronchioles) is more important to the success of the aforementioned medical tasks. As shown in Figure 1, although the red segment has higher voxel-wise accuracy (e.g., dice accuracy), the blue one shows more fine bronchioles and thus provides a better airway road map. In the case of COPD, small airway destruction and narrowing are among the earliest pathological changes, leading to decreased lung function and exacerbation frequency [7]. Therefore, accurate segmentation of fine bronchioles is crucial for early diagnosis and monitoring of COPD.

Besides the morphological complexity, airway segmentation becomes more challenging because of the imbalance sizes among airways of different generations. The airway tree begins from the trachea and ends at the alveoli. The trachea beginning

at the larynx is denoted as *Generation 0*, while its subsequently divided left and right main-stem bronchi as *Generation 1*. The airways become progressively finer until the 23rd generation—alveolar sacs [9]. In our paper, *low generation* stands for large airways closer to the trachea, while *high generation* refers to fine bronchioles closer to the alveolar sacs. As shown in Figure 1, low-generation airways occupy most of the voxels but have fewer branches compared to high-generation airways. Voxel-wise loss functions such as dice loss may lead to the failure of segmenting fine bronchioles. While training on low-generation airways and then on high-generation airways may partly solve the problem [10], this scheme causes the model to lose knowledge of low-generation airways after long training on high-generation airways.

Over the years, many automated airway segmentation methods have been developed. There are two main categories—traditional methods which rely on manually selected features [11]–[24] and deep learning-based methods which combine deep learning models with traditional methods or focus on new model architecture design [8], [10], [25]–[45]. However, effective approaches to guaranteeing topological accuracy and addressing the challenge of imbalanced sizes remain lacking.

Therefore, we present a method, coined as **NaviAirway**, which is a training framework that can be built on any backbone model. For airway topology preservation, we design a bronchiole-sensitive loss function by pushing the model to recognize fine bronchioles. For accurate model learning across different airway generations, we propose a human-vision-inspired iterative training strategy by guiding the model to specifically extract features of both low- and high-generation airways and preserve those learned features. To further enhance the learning of airway branch features, inspired by Noisy Student [46], we present a teacher-student training method to distill the knowledge from numerous unlabeled CT chest images and increase model accuracy and robustness.

To evaluate model performance, we first test NaviAirway on two public datasets. The comparison results show that our method is more accurate and detects longer airway trees than existing methods. We subsequently test NaviAirway on a private dataset, demonstrating its robustness to a previously unexposed dataset.

Our contributions are summarized as follows:

- To our best knowledge, NaviAirway presents the first in-depth study of airway segmentation training framework that focuses on topological correctness, instead of voxel-wise accuracy, and tackles the problems of branch size imbalance. Our method is general, effective, and compatible with any backbone model.
- We build a new bronchiole-sensitive loss function that guarantees topological accuracy and drives the model to recognize finer bronchioles (i.e., fine and long tubular shapes), and a new human-vision-inspired iterative training strategy that guides the model to learn both the features of fine and coarse airways while preventing knowledge loss of airway features.

II. RELATED WORKS

A. Traditional Methods

Traditional methods mainly include 1) region growing and thresholding, 2) morphologic and geometric model-based methods, and 3) hybrid approaches combining the above two methods [11], [12]. For example, EXACT’09 Challenge [13] presented 15 airway tree extraction algorithms submitted to the competition. Ten out of the 15 methods used region growing and thresholding techniques which utilize brightness of different tissues. Similar techniques were also developed, including pixel value filtering and thresholding [14], thresholding and rectangular region mask [15], GVF snakes [16], fuzzy connectivity [17], [18], and two-pass region growing [19]. Alternatively, airways were mathematically defined according to their morphologic and geometric features of airway for extraction [20], [21]. Hybrid methods combined the strengths of the two to provide better segmentation [22]–[24].

B. Deep Learning-based Methods

Compared with traditional methods, deep learning-based models, on average, detect twice longer airways [26], [27], [30]–[32], [35], [37], [40]–[45], [47]–[49]. Abundant studies combined Convolutional Neural Networks (CNNs) and traditional methods based on the idea that CNN provided preliminary results, and the traditional method was responsible for refinement. One mainstream of studies used 3D U-Net [25] as the backbone model and built different post-processing approaches, including fuzzy connectedness region growing and skeletonization guided leakage removal [26], image boundary post-processing to minimize the boundary effect in airway reconstruction [27], and freeze-and-grow propagation [28]. Some works focused on designing the backbone network. A simple and low-memory 3D U-Net was proposed in [29]. Graph Neural Networks (GNNs) were adopted to segment airways [30], [31]. In [32], a GNN module was incorporated into a 3D U-Net, while [33] developed a graph refinement-based airway extraction method by combining GNN and mean-field networks. Beyond utilizing existing deep learning models which were built for general tasks, in more recent studies, new network architectures (usually based on 3D U-Net) considering special features of airways were designed to achieve a higher segmentation accuracy. They included patch classification by 2.5 CNN [34], AirwayNet [35], Airway-SE [36], 2D plus 3D CNN [10], attention distillation modules plus feature recalibration modules [8], [37], group supervision plus union loss function [38], attention on weak feature regions [39], BREAK [40], and CFDA [44]. Despite great progress made by deep learning-based methods, general and effective approaches to airway topology preservation while tackling the problem of size imbalance are lacking.

III. METHOD

Consider a labeled set $\mathcal{D} : \{(\mathbf{x}_i, \mathbf{a}_i)\}_{i=1}^N$, where \mathbf{x}_i is a 3D CT image, \mathbf{a}_i is the corresponding airway annotation map, and N is the number of labeled images. Note that \mathbf{a}_i denotes each voxel on \mathbf{x}_i as either background or airway. Also, we

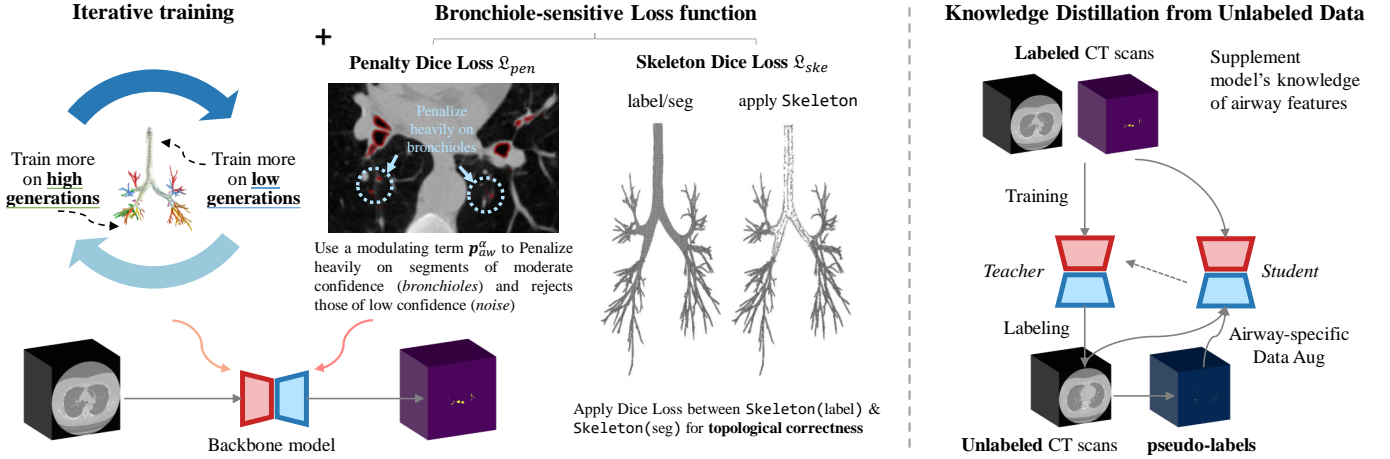


Fig. 2. Pipeline of NaviAirway. It consists of a bronchiole-sensitive loss function ($\mathcal{L}_{ske} + \mathcal{L}_{pen}$) that preserves airway topology, and an iterative training strategy that enhances the model’s learning across different airway generations. In addition, the model’s ability to learn airway features is further improved through knowledge distillation from unlabeled images.

have an unlabeled set $\mathcal{U} : \{\mathbf{x}_i\}_{i=1}^M$, where M is the number of unlabeled 3D CT images and $M \gg N$.

Our pipeline (see Figure 2) consists of a backbone model (Section III-A), a new bronchiole-sensitive loss function (Section III-B), and a new human-vision-inspired iterative training strategy (Section III-C). Then, a teacher-student training technique (Section III-D) further distills the knowledge of airway branch features to increase model robustness. Finally, we introduce our simple post-processing procedure (Section III-E).

A. Backbone Model: Feature Extraction from a Larger Area

Our method offers great flexibility as the backbone model architecture can be customized according to the specific needs of different applications. For our implementation, we design the model, denoted as Φ_θ , based on the well-established 3D U-Net architecture [25]. We introduce a novel feature extraction module, consisting of one dilated convolution, one self-attention block, and two typical convolutional kernels, to replace the conventional convolution kernels in the down-sampling and up-sampling operations. This innovative module enables the model to extract features from a larger surrounding area, thus preventing interference from other tubular shapes such as the esophagus and vessels, leading to better segmentation results.

B. Loss Function: Topological Correctness

Dice loss [50] is a commonly used loss function for image segmentation that calculates voxel-wise accuracy (see Equation (1)). However, in our case, preserving the topological correctness of the airway is our primary concern. Therefore, we propose our own loss function based on the dice loss

$$\text{Dice}(\mathbf{p}, \mathbf{a}, \mathbf{w}) = 1 - \frac{2 \sum_{k=1}^K p_k a_k w_k}{\sum_{k=1}^K p_k^2 + \sum_{k=1}^K a_k^2}, \quad (1)$$

where \mathbf{p} denotes the model prediction; \mathbf{a} denotes the reference label; \mathbf{w} is a weight value; k denotes the voxel position; K is

the total number of voxels; $p_k \in [0, 1]$ is the model confidence of a voxel being background or airway, while $a_k \in \{0, 1\}$ is the computer-assisted manual annotation of the k -th voxel, where the voxel being the background is assigned as 0 and the voxel being the airway is given a 1.

We use the idea of skeletonization to evaluate topological correctness. Skeletonization is a process which reduces binary images to one-voxel-wide skeletons. If the skeletons of the predicted airway match with the reference labels, the topology is deemed to be successfully preserved. However, current skeletonization methods [51] remain a discrete operation, which cannot be applied to a differentiable approximation process. Moreover, the size imbalance among airways of different generations makes skeleton extraction more challenging.

To address this, we present our differentiable semi-skeletonization method, denoted as *Skeleton*. We use the morphological operations of erosion and dilation to extract an airway “skeleton” that is not strictly one-voxel wide but is enough for topological accuracy calculation. Specifically, we use MinPooling to erode and MaxPooling to dilate (for our implementation, the kernel size $ker = 3$). One iteration of erosion and dilation identifies some fine structures. After multiple iterations (for our implementation, $J = 3$), an airway “skeleton” is extracted (Figure 2). Our **Skeleton Dice Loss** \mathcal{L}_{ske} is formulated as shown in Equation (2).

$$\mathcal{L}_{ske} = \text{Dice}(\text{Skeleton}(\mathbf{p}_{aw}), \text{Skeleton}(\mathbf{a}_{aw}), \mathbf{1}), \quad (2)$$

where subscripts aw denotes the prediction / annotation of airway; *Skeleton* is from Algorithm 1, and see *Dice* in Equation (1).

However, relying solely on Skeleton Dice Loss may not be sufficient as overall accuracy is equally important as topological accuracy. To address this issue, we have designed the **Penalty Dice Loss** \mathcal{L}_{pen} (see Equation (3)), which includes a modulating term \mathbf{p}_{aw}^α to encourage the model to perform better on challenging cases. Since the confidence scores of bronchiole voxels or voxels near the surface between airway

Algorithm 1: Differentiable semi-skeletonization

Input: An image \mathbf{m} in which lower values denote background while higher values denote foreground, kernel size ker , number of iterations J .

Init: Skeleton $\mathbf{s} \leftarrow$ a zero image with the same shape as \mathbf{m} , padding size $pad \leftarrow \frac{1}{2}(ker - 1)$.

- 1 **Function** Skeleton(\mathbf{m}):
- 2 **repeat**
- 3 $\hat{\mathbf{m}} \leftarrow$ Dilate(Erode(\mathbf{m}));
- 4 $\mathbf{s} \leftarrow$ ReLU($\mathbf{m} - \hat{\mathbf{m}}$) + \mathbf{s} ;
- 5 $\mathbf{m} \leftarrow$ Erode($\hat{\mathbf{m}}$);
- 6 **until** Finishing J iterations;
- 7 **return** \mathbf{s} ;
- 8 **Function** Erode(\mathbf{m}):
- 9 **return** MinPool(\mathbf{m} , ker , pad);
- 10 **Function** Dilate(\mathbf{m}):
- 11 **return** MaxPool(\mathbf{m} , ker , pad);

branches and background tend to be relatively low, this loss function penalizes the model more heavily for misclassifying such voxels. As the backbone model outputs two prediction maps of the airway and background after the softmax operation, \mathcal{L}_{pen} is composed of two components:

$$\begin{aligned} \mathcal{L}_{pen} &= \mathcal{L}_{pen}^{aw} + \mathcal{L}_{pen}^{bg}, \\ \mathcal{L}_{pen}^{aw} &= \text{Dice}(\mathbf{p}_{aw}^\alpha, \mathbf{a}_{aw}, \mathbf{w}_{aw}), \\ \mathcal{L}_{pen}^{bg} &= \text{Dice}(\mathbf{p}_{bg}, \mathbf{a}_{bg}, \mathbf{1}), \end{aligned} \quad (3)$$

where subscripts / superscript bg denotes the prediction / annotation of background; \mathbf{w}_{aw} is assigned by the thickness of airway branches; α is an integer and \mathbf{p}_{aw}^α is the modulating term representing every element p_k to the power of α (in this paper, $\alpha = 2$).

To address the hard case problem in image segmentation, traditional methods assign larger weights to those difficult cases to improve performance, as shown in Equation (1). However, these hand-designed weights are not adaptable during training, which limits their effectiveness. In contrast, we propose a dynamic modulating term, \mathbf{p}_{aw}^α , which acts as a pseudo-confidence score for difficult cases.

During training, suppose α is 2, for a voxel with $p_k = 0.5$ with its target score being 1, the resulting p_k^2 value is only 0.25. Therefore, the model is encouraged to predict a p_k value larger than 0.7, resulting in a pseudo-confidence score greater than 0.5 for being an airway. In contrast, during inference, we only use p_k to determine airway segments. This approach is akin to athletes training with additional weights to build strength and then removing them during competition. More analysis and discussion of the Penalty Dice Loss will be presented in Section V-2.

The final loss function is the sum of \mathcal{L}_{ske} and \mathcal{L}_{pen} .

C. Iterative Training Strategy: Solution to Size Imbalance

We address the issue of size imbalance in our segmentation problem, where lower airway generations contain significantly more voxels than higher generations, as shown in Figure 1. To train our model on this imbalanced data, we first crop the CT

images into cuboids and feed them into the model in batches. However, if all cuboids are chosen with the same frequency, the resulting class distribution is severely unbalanced, with few samples for high generations. To overcome this problem, we propose an iterative training strategy inspired by sampling techniques used in class imbalance problems [52].

In our strategy, we adjust the probability of selecting each cuboid pair $(\mathbf{x}_i^j, \mathbf{a}_i^j)$ in a batch, based on the ratio r_i^j of the number of outermost voxels of the airway segment to the total number of airway voxels, representing the reciprocal of the radius. Larger r_i^j indicates that the airways in \mathbf{a}_i^j are fine bronchioles, while smaller r_i^j indicates larger airways. In each iteration, we train the model on both high and low generations, but with different frequencies. Specifically, when the probability of selecting a cuboid pair is proportional to r_i^j (scaled by a temperature parameter τ_h), the model is trained more frequently on high generations (h iter in Equation (4)). Conversely, when the probability is inversely proportional to r_i^j (scaled by a temperature parameter τ_l), the model is trained more frequently on low generations (l iter in Equation (4)). If $r_i^j = \infty$, indicating no airway exists in the cuboid, we assign a constant probability value β_0 (in this paper, $\beta_0 = 1$). We apply a softmax function to normalize the probabilities and use temperature scaling to control the degree of imbalance.

By adjusting the sampling frequencies based on the ratio of outermost airway voxels to the total airway voxels, our iterative training strategy addresses the size imbalance problem in airway segmentation.

$$p_i^j = \begin{cases} \frac{\exp(r_i^j/\tau_h)}{\sum_{r_i^j \neq \infty} \exp(r_i^j/\tau_h) + \sum_{r_i^j = \infty} \exp(\beta_0/\tau_h)} & (h \text{ iter}) \\ \frac{\exp(1/(\tau_l r_i^j))}{\sum_{r_i^j \neq \infty} \exp(1/(\tau_l r_i^j)) + \sum_{r_i^j = \infty} \exp(\beta_0/\tau_l)} & (l \text{ iter}) \end{cases}, \quad (4)$$

where p_i^j represents the probability of the sampled cuboid pair $(\mathbf{x}_i^j, \mathbf{a}_i^j)$ in a training batch; τ_h and τ_l are two manually selected temperature values (in this paper, $\tau_h = 1$, $\tau_l = 0.1$). We will present more analysis of our proposed training strategy in Section V-1.

D. Knowledge Distillation from Unlabeled Data

In many cases, we have a larger number of unlabeled images \mathcal{U} than labeled ones \mathcal{D} , meaning M is much greater than N . To leverage the vast amount of unlabeled data, we propose a teacher-student training framework (inspired by Noisy Student [46]) to distill the knowledge of the CT chest image distribution [53] and enhance model accuracy and robustness (see Algorithm 2). Our approach also incorporates airway-specific data augmentation to further enhance the distillation process.

E. Post Processing

This step aims at identifying and removing any disconnected noise shapes. After model training, we obtain an airway

Algorithm 2: Distill knowledge from unlabeled data

Input: An optimized model Φ_{θ^*} trained on labeled dataset \mathcal{D} , an unlabeled dataset \mathcal{U} ($M \gg N$), two probability values, q^t and q^c , used for data augmentation, number of iterations I .

Init: Teacher model $\Phi_{\theta^T} \leftarrow \Phi_{\theta^*}$, student model $\Phi_{\theta^S} \leftarrow \Phi_{\theta^*}$, divide \mathcal{U} into V batches $\{\mathcal{U}_b\}_{b=1}^V$ (where $V \sim N$).

1 Function `AirwayPseudoLabel` (\mathbf{x}_i, q^t, q^c):

2 $\mathbf{A}_i \leftarrow \Phi_{\theta^T}(\mathbf{x}_i) > t$ ($t = 0.5$ with probability of q^t , otherwise $t = 0.7$);

3 $\mathbf{A}_i \leftarrow \mathcal{S}_{h^*}$ with probability of q^c (see Sec. III-E for the definition of \mathcal{S}_{h^*});

4 **return** \mathbf{A}_i ;

5 repeat

6 **for** $\mathcal{U}_b \in \{\mathcal{U}_b\}_{b=1}^V$ **do**

7 **for** $\mathbf{x}_i \in \mathcal{U}_b$ **do**

8 $\mathbf{A}_i \leftarrow \text{AirwayPseudoLabel}(\mathbf{x}_i, q^t, q^c)$;

9 Add \mathbf{A}_i to \mathcal{U}_b ;

10 Train Φ_{θ^S} on $\{\mathcal{D} + \mathcal{U}_b\}$;

11 $\Phi_{\theta^T} \leftarrow \Phi_{\theta^S}$;

12 until *Finishing* I iterations;

confidence map $\Phi_{\theta}(\mathbf{x})$. By applying a threshold value th , we can create an airway mask \mathbf{A} where $\mathbf{A} = \Phi_{\theta}(\mathbf{x}) > th$. Since airway branches are typically connected, we can assume that the largest connected shape in the output is the airway segmentation. Therefore, we identify the largest connected shape $\mathcal{S}_{h^*} = \max |\mathcal{S}_h|$ from the set of separated shapes $\{\mathcal{S}_h\}$ in \mathbf{A} . However, there may be some broken airway branches in the other separated shapes $\{\mathcal{S}_h\} \setminus \mathcal{S}_{h^*}$. We connect those broken branches to \mathcal{S}_{h^*} if they are close enough. To connect, we first define a search range R . For every end point e of airway branches in \mathcal{S}_{h^*} , if any shape $\mathcal{S}_{\hat{h}}$ in $\{\mathcal{S}_h\} \setminus \mathcal{S}_{h^*}$ is within $B_R(e)$ (i.e., the neighborhood of e), update \mathcal{S}_{h^*} by $\mathcal{S}_{h^*} := \mathcal{S}_{h^*} + \mathcal{S}_{\hat{h}}$, and make \mathcal{S}_{h^*} a connected shape by lowering threshold th within $B_R(e)$ to fill the gap. In our experiments, R is set to be small (e.g., $R = 2$ in this paper) as the broken branch connection is only for refinement purposes.

IV. EXPERIMENTS

A. Datasets

Three public datasets (*EXACT'09* [13], *Binary Airway Segmentation (BAS)* [8], and *Airway Tree Modeling Challenge (ATM22)* [35], [38], [40], [41]) and one private dataset (*QMH*) were used to evaluate NaviAirway. **1) EXACT'09.** It contains 20 CT images for training and 20 images for testing. The images have slice thickness ranging from 0.45mm to 1.0mm while the pixel spacing ranges from 0.5mm to 0.78mm. **2) BAS.** It has 90 images (20 from the training set of EXACT'09 [13] and 70 from LIDC-IDRI [38], [54]) associated with 90 corresponding manually-labeled annotations. The pixel spacing ranges from 0.5mm to 0.8mm, and the slice thickness ranges from 0.5mm to 1.0mm. We follow the instructions in [40] to split BAS into a training set, a validation set, and a test set. **3) ATM22.** The 300 training cases (with labels) and 50 validation cases (without labels) are publicly available. All the CT scans were selected from LIDC-IDRI

TABLE I
PERFORMANCE COMPARISON ON BAS DATASET.
MEAN \pm STANDARD DEVIATION (%) IS SHOWN FOR EACH METRIC.

	DSC	Sensitivity	BD	TD
Jin et al. [26]	93.6 \pm 2.0	88.1 \pm 8.5	93.1 \pm 7.9	84.8 \pm 9.9
Juarez et al. [27]	93.6 \pm 2.2	86.7 \pm 9.1	91.9 \pm 9.2	80.7 \pm 11.3
AG U-Net [30]	82.7 \pm 22.2	72.5 \pm 28.9	70.1 \pm 33.3	63.5 \pm 30.8
Wang et al. [31]	93.5 \pm 2.2	88.6 \pm 8.8	93.4 \pm 8.0	85.6 \pm 9.9
Juarez et al. [32]	87.5 \pm 13.2	77.5 \pm 15.5	77.5 \pm 20.9	66.0 \pm 20.4
AirwayNet [35]	93.7 \pm 1.9	87.2 \pm 8.9	91.6 \pm 8.3	82.1 \pm 10.9
Xue et al. [55]	92.1 \pm 2.4	-	87.7 \pm 8.1	88.2 \pm 6.9
Qin et al. [8]	91.5 \pm 2.9	-	87.6 \pm 9.2	91.8 \pm 5.3
Qin et al. [37]	92.5 \pm 2.0	93.6 \pm 5.0	96.2\pm5.8	90.7 \pm 6.9
Zheng et al. [38]	91.4 \pm 3.3	-	88.7 \pm 7.9	92.5 \pm 4.5
Ours (th=0.5)	92.7 \pm 1.6	98.9\pm1.3	94.4 \pm 10.1	96.2\pm4.9
Ours (th=0.7)	95.1\pm1.2	97.3 \pm 2.1	85.4 \pm 11.7	92.1 \pm 8.5

TABLE II
PERFORMANCE COMPARISON ON EXACT'09 DATASET.
MEAN \pm STANDARD DEVIATION IS SHOWN FOR EACH METRIC.

	Branch	Length (cm)	BD (%)	TD (%)
Xu et al. [56]	128.7 \pm 60.3	94.8 \pm 44.7	51.7 \pm 10.8	44.5 \pm 9.4
Yun et al. [34]	163.4 \pm 79.4	129.3 \pm 66.0	65.7 \pm 13.1	60.1 \pm 11.9
Qin et al. [37]	190.4	166.5	76.7 \pm 11.5	72.7 \pm 11.6
Zheng et al. [38]	199.9	180.9	80.5 \pm 12.5	79.0 \pm 11.1
DTPDT [57]	203.9	182.4	82.1 \pm 10.6	79.6 \pm 9.5
Neko [47]	84.5 \pm 40.5	61.9 \pm 30.9	35.5 \pm 8.2	30.4 \pm 7.4
UCCTeam [48]	99.0 \pm 50.3	75.1 \pm 39.4	41.6 \pm 9.0	36.5 \pm 7.6
FF_ITC [49]	198.3 \pm 98.6	177.1 \pm 97.0	79.6 \pm 13.5	79.9 \pm 12.1
MISLAB [13]	104.7 \pm 55.2	78.7 \pm 41.7	42.9 \pm 9.6	37.5 \pm 7.1
NTNU [58]	72.4 \pm 37.8	54.3 \pm 33.9	31.3 \pm 10.4	27.4 \pm 9.6
Ours (th=0.5)	219.3\pm65.5	196.6\pm53.9	88.3\pm24.3	85.6\pm20.0

[54] and the Shanghai Chest hospital and were labeled by deep learning models and radiologists' manual correction. **4) QMH.** Nine cases with slice thicknesses ranging from 1.0mm to 5.0mm and pixel spacings ranging from 0.5 to 0.9 were labeled using commercial software named LungPoint with experts' manual correction. They were used for external testing because the data distribution was unseen by the model.

There were also a large number of unlabeled cases in LIDC-IDRI (which has 1018 cases in total) and QMH (which has 101 unlabeled cases). Those unlabeled data were used for knowledge distillation of airway branch features to increase model robustness.

B. Implementation

1) Data preparation: First, we stacked up the CT slices (in the DICOM format) to form 3D image data if needed. Then, thresholding was done to keep the Hounsfield Unit (HU) values within $[-1000, 600]$. The pixel values were further standardized to be within $[0, 1]$. During training, images were cropped into 32x128x128 cuboids owing to available GPU memory.

2) Training Procedure: We used PyTorch [59] to implement our model. Data augmentation, including random flip, random affine, random blur, random noise, random motion, and random spike [60], was performed to expand the sample size. The model was trained on two NVIDIA GeForce RTX 2080 Ti cards with an Adam optimizer and a learning rate of

TABLE III
ABLATION STUDY ON BAS DATASET. MEAN \pm STANDARD DEVIATION (%) IS SHOWN FOR EACH METRIC.

Backbone	\mathcal{L}_{pen}	\mathcal{L}_{ske}	Iter Train	Distill	Data Aug	DSC	Sensitivity	BD	TD
✓					✓	92.6 \pm 1.4	94.7 \pm 3.6	65.9 \pm 17.8	66.5 \pm 19.8
✓	✓				✓	92.0 \pm 1.6	95.2 \pm 3.9	71.4 \pm 14.7	77.7 \pm 17.8
✓		✓			✓	92.4 \pm 1.5	95.8 \pm 3.4	72.9 \pm 13.8	79.3 \pm 14.1
✓	✓	✓			✓	91.7 \pm 1.4	96.0 \pm 2.9	75.2 \pm 13.5	81.9 \pm 12.8
✓			✓		✓	92.5 \pm 1.4	95.6 \pm 3.5	71.7 \pm 13.9	76.5 \pm 15.1
✓	✓	✓	✓		✓	92.4 \pm 1.8	97.5 \pm 1.8	86.8 \pm 13.5	90.8 \pm 8.8
✓	✓	✓	✓	✓		93.1\pm1.5	97.7 \pm 1.8	90.8 \pm 9.6	92.9 \pm 4.6
✓	✓	✓	✓	✓	✓	92.7 \pm 1.6	98.9\pm1.3	94.4\pm10.1	96.2\pm4.9

“Backbone” represents the backbone model introduced in Section III-A; \mathcal{L}_{pen} and \mathcal{L}_{ske} are Penalty Dice Loss and Skeleton Dice Loss proposed in Section III-B; “Iter Train” represents the iterative training strategy in Section III-C; “Distill” represents the knowledge distillation module; “Data Aug” means the data augmentation applied to the training batches.

10^{-5} . To implement our iterative training, we sampled 1000 cuboids with one of the strategies (e.g., *l iter*) in Equation (4) and switched to the other strategy (e.g., *h iter*) after finishing one epoch. The total number of epochs was determined based on the size of the training dataset. For example, on the BAS dataset, we trained the model for 100 epochs.

C. Metrics

Ideally, the accuracy of model-based airway segmentation is best evaluated through the actual bronchoscopic procedure by experts. However, it is labor-intensive, and any additional examination that may prolong the clinical procedure should be avoided. Therefore, we only have *reference* labels, instead of *ground truth* labels. Hence, in cases of airway segmentation, the goal of a model is not to provide airway segments that perfectly match the reference but to recognize bronchioles as many as possible from CT images.

We adopted the Tree length Detected rate (TD) and Branch Detected rate (BD) from EXACT’09 [13] to evaluate topological accuracy. Additionally, we employed Dice Similarity Coefficient (DSC, $\frac{2TP}{2TP+FP+FN}$) to evaluate the overall similarity between model predictions and the reference labels. Sensitivity ($\frac{TP}{TP+FN}$) was used to check the percentage of volumes the model detects in the reference labels.

D. Performance comparison

First, shown in Table I and II, we compared NaviAirway with existing methods [8], [13], [26], [27], [30]–[32], [34], [35], [37], [38], [47]–[49], [55]–[58] on both BAS [8] and EXACT’09 [13] datasets. For the BAS dataset (Table I), our method outperformed others in both topological accuracy metrics (BD: 94.4 \pm 10.1 and TD: 96.2 \pm 4.9) and Sensitivity (98.9 \pm 1.3). Note that “th” means the threshold value to decide whether a voxel in the prediction map belongs to the airway or not. Here we show the results of two threshold values, 0.5 and 0.7. As shown in Figure 3, when th=0.5, our NaviAirway detects more bronchioles which are not shown in the reference label and are previously regarded as “false positive” predictions. However, as mentioned in Section IV-C, the reference labels may miss some airways due to the limitation of manual labeling. After the exam by a bronchologist, these “extra bronchioles” are considered to be true. That is why “th=0.5”

has a lower DSC value than “th=0.7”. A lower DSC does not necessarily mean the performance is worse as there might be missed airways in the reference labels. On average, our method detects bronchioles up to the 12th generation, whereas the mean and median values of the detected generation number are 7.9 and 7.5, respectively.

Table II shows the performance comparison on the EXACT’09 dataset. In this table, “Branch” represents the number of airway branches and “Length” is detected airway length in cm. Our NaviAirway detects the longest airway (196.6 \pm 53.9) and up to the 13th generation on average while having the highest BD (88.3 \pm 24.3) and TD (85.6 \pm 20.0).

Moreover, we also tested our method in the ATM22 challenge [35], [38], [40], [41]. Among the submissions in the long-term validation phase, NaviAirway achieved the third highest BD (95.5) and the second highest TD (96.3). Note that we adopted the same set of hyperparameters for the training of the three datasets (BAS, EXACT’09, and ATM22).

E. Ablation study

We conducted all ablation studies on the BAS dataset to evaluate the contribution of each component in our proposed model to performance improvement. Additionally, we tested various settings of hyperparameters in each component to further optimize the model’s performance.

1) *The effectiveness of bronchiole-sensitive loss function:* Step by step, we verified the effectiveness of NaviAirway. As shown in Table III, compared with the baseline case (“Backbone”), Penalty Dice Loss \mathcal{L}_{pen} alone boosted the performance from 65.9 BD and 66.5 TD to 71.4 (+5.5) BD and 77.7 (+11.2) TD, and Skeleton Dice Loss \mathcal{L}_{ske} alone boosted the performance from 65.9 BD and 66.5 TD to 72.9 (+7.0) BD and 79.3 (+12.8) TD. When combining \mathcal{L}_{pen} and \mathcal{L}_{ske} , the accuracy increased to 75.2 (+9.3) BD and 81.9 (+15.4) TD.

2) *The effectiveness of iterative training:* The iterative training strategy alone (see the row of “Backbone” + “Iter Train” in Table III) improved the baseline model by +5.8 BD and +10.0 TD, respectively. When combining iteration training and proposed loss functions, the performance was further boosted to 86.8 (+20.9) BD and 90.8 (+24.2) TD.

3) *The effectiveness of knowledge distillation from unlabeled images:* On top of \mathcal{L}_{pen} , \mathcal{L}_{ske} , and the proposed iterative

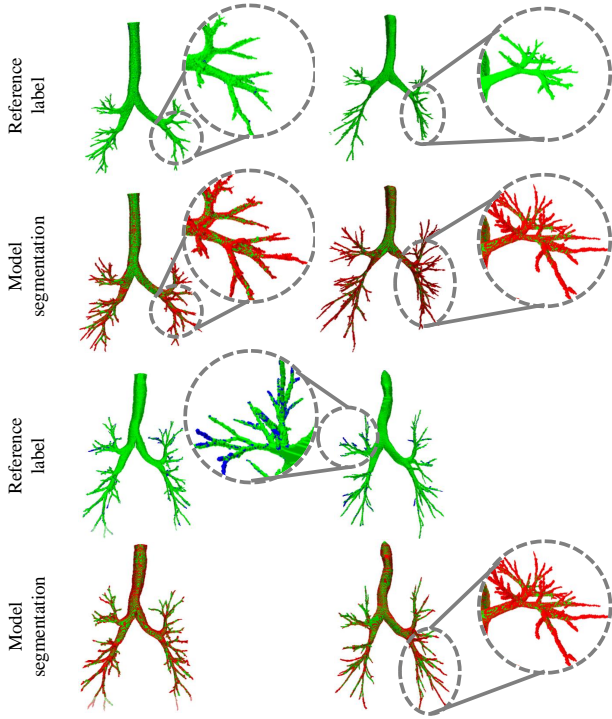


Fig. 3. Exemplary test results on BAS and EXACT’09 datasets showing that NaviAirway achieves high topological accuracy while finding more finer bronchioles than reference labels. (Green: overlapped volume. Red: extra airway voxels found by the model. Blue: missed airway voxels by the model.)

training strategy, knowledge distillation from unlabeled images could further increase the model performance to 94.4 (+7.6) BD and 96.2 (+5.4) TD. Additionally, comparing the last two rows, we found that data augmentation only had a minor effect on performance improvement. This indicates that the performance gain mainly comes from our proposed modules.

TABLE IV

STUDY ON HYPERPARAMETER SELECTION OF THE LOSS FUNCTION. MEAN \pm STANDARD DEVIATION (%) IS SHOWN FOR EACH METRIC.

	DSC	Sensitivity	BD	TD
$\alpha = 3$	93.2 \pm 2.1	97.3 \pm 1.5	92.5 \pm 9.1	94.3 \pm 5.3
$ker = 5$	92.9 \pm 1.4	98.2 \pm 1.6	94.6 \pm 10.9	95.9 \pm 5.0
$J = 1$	93.6 \pm 2.0	98.0 \pm 1.2	93.9 \pm 9.8	94.9 \pm 5.1
$J = 2$	93.0 \pm 1.5	98.4 \pm 1.4	94.3 \pm 10.0	96.4 \pm 4.9
$J = 4$	92.6 \pm 1.6	98.8 \pm 1.2	94.2 \pm 10.2	96.2 \pm 5.0
Default ¹	92.7 \pm 1.6	98.9 \pm 1.3	94.4 \pm 10.1	96.2 \pm 4.9

¹ “Default” represents our default setting where $\alpha = 2$, $ker = 3$, and $J = 3$. Other rows represent that only one hyperparameter varies at a time (e.g., $\alpha = 3$ represents the hyperparameter setting is $\alpha = 3$, $ker = 3$, and $J = 3$).

4) *Modulating term, kernel size, and number of iterations in loss function:* For Penalty Dice Loss \mathcal{L}_{pen} , we used α to control the modulating effect. Table IV shows the two cases of α : 2 and 3. We set $\alpha = 2$ by default. Besides, for Skeleton Dice Loss, the kernel size ker and the number of iteration(s) J (see Algorithm 1) determine the quality of skeletonization. We tested the cases where ker is 3 or 5 and J ranged from 1 to 4. We finally set $ker = 3$ and $J = 3$ because this setting led to satisfactory performance and computational efficiency.

TABLE V
COMPARISON OF DIFFERENT TRAINING STRATEGIES.

Strategy	DSC (%)	Strategy	DSC (%)
l iter only ($\tau_l = 1$)	89.6	First l iter then h iter	90.0
l iter only ($\tau_l = 0.1$)	90.4	First h iter then l iter	88.2
h iter only ($\tau_h = 1$)	87.3	Same frequency	92.6
h iter only ($\tau_h = 0.1$)	~ 0	Iterative	95.1

TABLE VI

GENERALITY OF NAVIAIRWAY (TESTED ON BAS DATASET). MEAN \pm STANDARD DEVIATION (%) IS SHOWN FOR EACH METRIC.

	DSC	Sensitivity	BD	TD
3D U-Net [25]	92.9 \pm 1.7	95.8 \pm 2.3	66.5 \pm 18.8	72.3 \pm 18.8
w/ NaviAirway	90.5 \pm 1.5	97.3 \pm 2.2	81.0 \pm 12.2	85.5 \pm 10.5
V-Net [50]	85.9 \pm 3.4	81.8 \pm 7.0	34.2 \pm 9.1	35.0 \pm 9.8
w/ NaviAirway	87.3 \pm 2.5	83.6 \pm 6.5	67.8 \pm 12.5	74.6 \pm 8.7
VoxResNet [61]	85.8 \pm 6.3	78.3 \pm 9.8	29.8 \pm 9.9	33.1 \pm 10.2
w/ NaviAirway	88.7 \pm 4.6	83.0 \pm 7.2	70.3 \pm 14.8	77.7 \pm 10.1
Wang et al. [31]	93.5 \pm 2.2	88.6 \pm 8.8	93.4 \pm 8.0	85.6 \pm 9.9
w/ NaviAirway	92.1 \pm 3.7	90.0 \pm 8.3	93.8 \pm 7.5	91.9 \pm 8.8

5) *Comparison of training strategies:* In Table V, we investigated different β values and compared the four training strategies (the right two columns) with the threshold being 0.7. Results show that our iterative training strategy performs the best.

F. Method generality

Our NaviAirway method can be generalized to other backbone models. As shown in Table VI, we simply applied NaviAirway to 3D U-Net [25], V-Net [50], VoxResNet [61], and Wang et al. [31] without careful hyperparameter tuning. The Results show that NaviAirway boosts the four models by a considerable margin. Additionally, Table VII examines the performance of our model in the unseen dataset (QMH). NaviAirway still achieves high accuracy (Sensitivity: 95.4, BD: 90.2, and TD: 83.7), indicating our method is robust to new data.

V. DISCUSSION

1) *Tackling the size imbalance problem by sampling techniques:* In Section III-C, we devised our strategy based on the ratio r_i^j , which can be interpreted as the ratio of surface area to volume of a given airway branch of interest. Since airway branches are long tubular structures, r_i^j can be approximated as $r_i^j \approx \frac{2\pi\hat{r}l}{\pi\hat{r}^2l} = \frac{2}{\hat{r}}$, where \hat{r} denotes the average radius and l denotes the average branch length. The size imbalance problem arises from the uneven distribution of airway branch volumes. The size of low-generation airways is approximately $(\frac{\hat{r}_l}{\hat{r}_h})^2$ (where subscript l means low and subscript h means high) times larger than those of high generations. Therefore, we use r_i^j to down- or up-sample the CT image cuboids. There are various approaches to sampling theoretically, and we presented an effective approach. In future work, we plan to conduct more in-depth investigations and explore alternative strategies.

TABLE VII
PERFORMANCE ON UNSEEN PRIVATE DATASET (QMH)
MEAN \pm STANDARD DEVIATION (%) IS SHOWN FOR EACH METRIC.

DSC	Sensitivity	BD	TD
86.3 \pm 4.9	95.5 \pm 1.3	90.6 \pm 8.2	84.3 \pm 25.3

TABLE VIII
REVIEW METRICS FOR AIRWAY SEGMENTATION.
MEAN \pm STANDARD DEVIATION (%) IS SHOWN FOR EACH METRIC.

Dataset	ABD ¹	ATD ²
BAS	114.2 \pm 18.1	113.2 \pm 17.5
QMH	132.4 \pm 24.5	108.6 \pm 13.5

¹ ABD: Adjusted Branch Detected.

² ATD: Adjusted Tree-length Detected.

2) *Interpreting Penalty Dice Loss*: To better understand the proposed loss function, we can analyze the derivative of \mathcal{L}_{pen} (Equation (3)). For p_k on the airway prediction map, $\frac{\partial \mathcal{L}_{pen}}{\partial p_k} = \frac{\partial \mathcal{L}_{pen}^{aw}}{\partial p_k}$, while on the background prediction map, $\frac{\partial \mathcal{L}_{pen}}{\partial p_k} = \frac{\partial \mathcal{L}_{pen}^{bg}}{\partial p_k}$. As shown in Figure 4, $\frac{\partial \mathcal{L}_{pen}^{bg}}{\partial p_k}$ follows a linear pattern, whereas $\frac{\partial \mathcal{L}_{pen}^{aw}}{\partial p_k}$ indicates that \mathcal{L}_{pen}^{aw} penalizes heavily on airway segments of moderate confidence (which could be bronchioles) and rejects those of too low confidence (which tend to be noises).

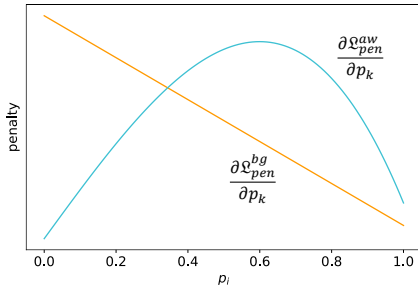


Fig. 4. The changes of $\frac{\partial \mathcal{L}_{pen}^{aw}}{\partial p_k}$ and $\frac{\partial \mathcal{L}_{pen}^{bg}}{\partial p_k}$ with different p_k values. The blue curve shows that \mathcal{L}_{pen}^{aw} penalizes heavily on airway segments of moderate confidence and rejects those of too low confidence.

3) *Complementary Metrics Needed*: Most existing works followed the metrics built in the EXACT’09 challenge in 2009 [13]. However, because we only have the “reference” labels, instead of the “ground truth” segmentation, complementary metrics are needed. First, quantitative evaluation was insufficient. We proposed to include visual inspection because some “False Positive (FP) airway segments” might be true airway branches that were missed by the “reference” labels. As shown in Table VIII, we refine Branch Detected (BD) and Tree-length Detected (TD) to be the ratio between “True Positive (TP) airway segments” plus true airway segments missed by “reference” labels over the segments in “reference” labels and denote the two adjusted metrics as Adjusted Branch Detected (ABD) and Adjusted Tree-length Detected (ATD). Results show that NaviAirway helped the model learn the general features of airways, so the model could detect more finer bronchioles that were not shown in the “reference” labels.

VI. CONCLUSIONS

In this paper, we present a novel airway segmentation pipeline that provides extensive airway road maps with more detailed bronchioles. This is achieved through our proposed bronchiole-sensitive loss function for airway topology preservation and an iterative training strategy to address the size imbalance problem. Additionally, we leverage unlabeled chest CT images to distill airway branch features using a teacher-student training framework. Our approach is robust and outperforms existing methods on new CT scans from different systems and institutions. Furthermore, our method is compatible with various backbone models, thus improving their performance. Beyond airway segmentation, our approach can be extended to segmenting other fine and long tubular structures in biomedical images.

ACKNOWLEDGMENTS

REFERENCES

- [1] S. R. Deans, *The Radon transform and some of its applications*. Courier Corporation, 2007.
- [2] T. Ishiwata, A. Gregor, T. Inage, and K. Yasufuku, “Bronchoscopic navigation and tissue diagnosis,” *General thoracic and cardiovascular surgery*, vol. 68, no. 7, pp. 672–678, 2020.
- [3] E. Edell and D. Krier-Morrow, “Navigational bronchoscopy: Overview of technology and practical considerations—new current procedural terminology codes effective 2010,” *Chest*, vol. 137, no. 2, pp. 450–454, 2010.
- [4] F. Asano, R. Eberhardt, and F. J. Herth, “Virtual bronchoscopic navigation for peripheral pulmonary lesions,” *Respiration*, vol. 88, no. 5, pp. 430–440, 2014.
- [5] S. V. Kemp, “Navigation bronchoscopy,” *Respiration*, vol. 99, no. 4, pp. 277–286, 2020.
- [6] P. Berger, V. Perot, P. Desbarats, J. M. Tunon-de Lara, R. Marthan, and F. Laurent, “Airway wall thickness in cigarette smokers: quantitative thin-section ct assessment,” *Radiology*, vol. 235, no. 3, pp. 1055–1064, 2005.
- [7] A. Agustí and J. C. Hogg, “Update on the pathogenesis of chronic obstructive pulmonary disease,” *New England Journal of Medicine*, vol. 381, no. 13, pp. 1248–1256, 2019.
- [8] Y. Qin, H. Zheng, Y. Gu, X. Huang, J. Yang, L. Wang, and Y.-M. Zhu, “Learning bronchiole-sensitive airway segmentation cnns by feature recalibration and attention distillation,” in *International Conference on Medical Image Computing and Computer-Assisted Intervention*. Springer, 2020, pp. 221–231.
- [9] W. O. Reece, “Overview of the respiratory system,” *Dukes’ physiology of domestic animals*, vol. 203, 2015.
- [10] H. Zhang, M. Shen, P. L. Shah, and G.-Z. Yang, “Pathological airway segmentation with cascaded neural networks for bronchoscopic navigation,” in *2020 IEEE International Conference on Robotics and Automation (ICRA)*. IEEE, 2020, pp. 9974–9980.
- [11] E. M. Van Rikxoort and B. Van Ginneken, “Automated segmentation of pulmonary structures in thoracic computed tomography scans: a review,” *Physics in Medicine & Biology*, vol. 58, no. 17, p. R187, 2013.
- [12] J. Pu, S. Gu, S. Liu, S. Zhu, D. Wilson, J. M. Siegfried, and D. Gur, “Ct based computerized identification and analysis of human airways: a review,” *Medical physics*, vol. 39, no. 5, pp. 2603–2616, 2012.
- [13] P. Lo, B. Van Ginneken, J. M. Reinhardt, T. Yavarna, P. A. De Jong, B. Irving, C. Fetita, M. Ortner, R. Pinho, J. Sijbers *et al.*, “Extraction of airways from ct (exact’09),” *IEEE Transactions on Medical Imaging*, vol. 31, no. 11, pp. 2093–2107, 2012.
- [14] D. Aykac, E. A. Hoffman, G. McLennan, and J. M. Reinhardt, “Segmentation and analysis of the human airway tree from three-dimensional x-ray ct images,” *IEEE transactions on medical imaging*, vol. 22, no. 8, pp. 940–950, 2003.
- [15] H. Shi, W. C. Scarfe, and A. G. Farman, “Upper airway segmentation and dimensions estimation from cone-beam ct image datasets,” *International Journal of Computer Assisted Radiology and Surgery*, vol. 1, no. 3, pp. 177–186, 2006.

- [16] I. Cheng, S. Nilufar, C. Flores-Mir, and A. Basu, "Airway segmentation and measurement in ct images," in *2007 29th Annual International Conference of the IEEE Engineering in Medicine and Biology Society*. IEEE, 2007, pp. 795–799.
- [17] J. Tschirren, E. A. Hoffman, G. McLennan, and M. Sonka, "Intrathoracic airway trees: segmentation and airway morphology analysis from low-dose ct scans," *IEEE transactions on medical imaging*, vol. 24, no. 12, pp. 1529–1539, 2005.
- [18] —, "Segmentation and quantitative analysis of intrathoracic airway trees from computed tomography images," *Proceedings of the American Thoracic Society*, vol. 2, no. 6, pp. 484–487, 2005.
- [19] A. Fabijańska, "Two-pass region growing algorithm for segmenting airway tree from mdct chest scans," *Computerized Medical Imaging and Graphics*, vol. 33, no. 7, pp. 537–546, 2009.
- [20] M. W. Graham, J. D. Gibbs, D. C. Cornish, and W. E. Higgins, "Robust 3-d airway tree segmentation for image-guided peripheral bronchoscopy," *IEEE transactions on medical imaging*, vol. 29, no. 4, pp. 982–997, 2010.
- [21] C. Fetita, M. Ortner, P.-Y. Brillet, F. Prêteux, P. Grenier *et al.*, "A morphological-aggregative approach for 3d segmentation of pulmonary airways from generic msct acquisitions," in *Proc. of Second International Workshop on Pulmonary Image Analysis*, 2009, pp. 215–226.
- [22] A. P. Kiraly, W. E. Higgins, G. McLennan, E. A. Hoffman, and J. M. Reinhardt, "Three-dimensional human airway segmentation methods for clinical virtual bronchoscopy," *Academic radiology*, vol. 9, no. 10, pp. 1153–1168, 2002.
- [23] Q. Meng, T. Kitasaka, Y. Nimura, M. Oda, J. Ueno, and K. Mori, "Automatic segmentation of airway tree based on local intensity filter and machine learning technique in 3d chest ct volume," *International journal of computer assisted radiology and surgery*, vol. 12, no. 2, pp. 245–261, 2017.
- [24] B. van Ginneken, W. Baggerman, and E. M. van Rikxoort, "Robust segmentation and anatomical labeling of the airway tree from thoracic ct scans," in *International Conference on Medical Image Computing and Computer-Assisted Intervention*. Springer, 2008, pp. 219–226.
- [25] Ö. Çiçek, A. Abdulkadir, S. S. Lienkamp, T. Brox, and O. Ronneberger, "3d u-net: learning dense volumetric segmentation from sparse annotation," in *International conference on medical image computing and computer-assisted intervention*. Springer, 2016, pp. 424–432.
- [26] D. Jin, Z. Xu, A. P. Harrison, K. George, and D. J. Mollura, "3d convolutional neural networks with graph refinement for airway segmentation using incomplete data labels," in *International workshop on machine learning in medical imaging*. Springer, 2017, pp. 141–149.
- [27] A. G.-U. Juarez, H. A. Tiddens, and M. de Bruijne, "Automatic airway segmentation in chest ct using convolutional neural networks," in *Image analysis for moving organ, breast, and thoracic images*. Springer, 2018, pp. 238–250.
- [28] S. A. Nadeem, E. A. Hoffman, J. C. Sieren, A. P. Comellas, S. P. Bhatt, I. Z. Barjaktarevic, F. Abtin, and P. K. Saha, "A ct-based automated algorithm for airway segmentation using freeze-and-grow propagation and deep learning," *IEEE Transactions on Medical Imaging*, vol. 40, no. 1, pp. 405–418, 2020.
- [29] A. Garcia-Uceda, R. Selvan, Z. Saghir, H. Tiddens, and M. de Bruijne, "Automatic airway segmentation from computed tomography using robust and efficient 3-d convolutional neural networks," *arXiv preprint arXiv:2103.16328*, 2021.
- [30] J. Schlemper, O. Oktay, M. Schaap, M. Heinrich, B. Kainz, B. Glocker, and D. Rueckert, "Attention gated networks: Learning to leverage salient regions in medical images," *Medical image analysis*, vol. 53, pp. 197–207, 2019.
- [31] C. Wang, Y. Hayashi, M. Oda, H. Itoh, T. Kitasaka, A. F. Frangi, and K. Mori, "Tubular structure segmentation using spatial fully connected network with radial distance loss for 3d medical images," in *International Conference on Medical Image Computing and Computer-Assisted Intervention*. Springer, 2019, pp. 348–356.
- [32] A. G.-U. Juarez, R. Selvan, Z. Saghir, and M. de Bruijne, "A joint 3d unet-graph neural network-based method for airway segmentation from chest cts," in *International workshop on machine learning in medical imaging*. Springer, 2019, pp. 583–591.
- [33] R. Selvan, T. Kipf, M. Welling, A. G.-U. Juarez, J. H. Pedersen, J. Petersen, and M. de Bruijne, "Graph refinement based airway extraction using mean-field networks and graph neural networks," *Medical Image Analysis*, vol. 64, p. 101751, 2020.
- [34] J. Yun, J. Park, D. Yu, J. Yi, M. Lee, H. J. Park, J.-G. Lee, J. B. Seo, and N. Kim, "Improvement of fully automated airway segmentation on volumetric computed tomographic images using a 2.5 dimensional convolutional neural net," *Medical image analysis*, vol. 51, pp. 13–20, 2019.
- [35] Y. Qin, M. Chen, H. Zheng, Y. Gu, M. Shen, J. Yang, X. Huang, Y.-M. Zhu, and G.-Z. Yang, "Airwaynet: a voxel-connectivity aware approach for accurate airway segmentation using convolutional neural networks," in *International Conference on Medical Image Computing and Computer-Assisted Intervention*. Springer, 2019, pp. 212–220.
- [36] Y. Qin, Y. Gu, H. Zheng, M. Chen, J. Yang, and Y.-M. Zhu, "Airwaynet-se: A simple-yet-effective approach to improve airway segmentation using context scale fusion," in *2020 IEEE 17th International Symposium on Biomedical Imaging (ISBI)*. IEEE, 2020, pp. 809–813.
- [37] Y. Qin, H. Zheng, Y. Gu, X. Huang, J. Yang, L. Wang, F. Yao, Y.-M. Zhu, and G.-Z. Yang, "Learning tubule-sensitive cnns for pulmonary airway and artery-vein segmentation in ct," *IEEE Transactions on Medical Imaging*, vol. 40, no. 6, pp. 1603–1617, 2021.
- [38] H. Zheng, Y. Qin, Y. Gu, F. Xie, J. Yang, J. Sun, and G.-Z. Yang, "Alleviating class-wise gradient imbalance for pulmonary airway segmentation," *IEEE Transactions on Medical Imaging*, 2021.
- [39] W. Wu, Y. Yu, Q. Wang, D. Liu, and X. Yuan, "Upper airway segmentation based on the attention mechanism of weak feature regions," *IEEE Access*, vol. 9, pp. 95 372–95 381, 2021.
- [40] W. Yu, H. Zheng, M. Zhang, H. Zhang, J. Sun, and J. Yang, "Break: Bronchi reconstruction by geodesic transformation and skeleton embedding," in *2022 IEEE 19th International Symposium on Biomedical Imaging (ISBI)*. IEEE, 2022, pp. 1–5.
- [41] M. Zhang, X. Yu, H. Zhang, H. Zheng, W. Yu, H. Pan, X. Cai, and Y. Gu, "Fda: Feature decomposition and aggregation for robust airway segmentation," in *Domain Adaptation and Representation Transfer, and Affordable Healthcare and AI for Resource Diverse Global Health: Third MICCAI Workshop, DART 2021, and First MICCAI Workshop, FAIR 2021, Held in Conjunction with MICCAI 2021, Strasbourg, France, September 27 and October 1, 2021, Proceedings 3*. Springer, 2021, pp. 25–34.
- [42] Y. Gu, C. Gu, J. Yang, J. Sun, and G.-Z. Yang, "Vision-kinematics interaction for robotic-assisted bronchoscopy navigation," *IEEE Transactions on Medical Imaging*, vol. 41, no. 12, pp. 3600–3610, 2022.
- [43] H. Zheng, Y. Qin, Y. Gu, F. Xie, J. Sun, J. Yang, and G.-Z. Yang, "Refined local-imbalance-based weight for airway segmentation in ct," in *Medical Image Computing and Computer Assisted Intervention—MICCAI 2021: 24th International Conference, Strasbourg, France, September 27–October 1, 2021, Proceedings, Part I*. Springer, 2021, pp. 410–419.
- [44] M. Zhang, H. Zhang, G.-Z. Yang, and Y. Gu, "Cfda: Collaborative feature disentanglement and augmentation for pulmonary airway tree modeling of covid-19 cts," in *Medical Image Computing and Computer Assisted Intervention—MICCAI 2022: 25th International Conference, Singapore, September 18–22, 2022, Proceedings, Part I*. Springer, 2022, pp. 506–516.
- [45] Y. Wu, M. Zhang, W. Yu, H. Zheng, J. Xu, and Y. Gu, "Lts: long-term slice propagation for accurate airway segmentation," *International Journal of Computer Assisted Radiology and Surgery*, vol. 17, no. 5, pp. 857–865, 2022.
- [46] Q. Xie, M.-T. Luong, E. Hovy, and Q. V. Le, "Self-training with noisy student improves imagenet classification," in *Proceedings of the IEEE/CVF Conference on Computer Vision and Pattern Recognition*, 2020, pp. 10 687–10 698.
- [47] H. Balacey, "Mise en place d'une chaîne complète d'analyse de l'arbre trachéo-bronchique à partir d'examen (s) issus d'un scanner-ct: de la 3d vers la 4d," Ph.D. dissertation, Bordeaux 1, 2013.
- [48] P. Nardelli, K. A. Khan, A. Corvò, N. Moore, M. J. Murphy, M. Twomey, O. J. O'Connor, M. P. Kennedy, R. S. J. Estépar, M. M. Maher *et al.*, "Optimizing parameters of an open-source airway segmentation algorithm using different ct images," *Biomedical engineering online*, vol. 14, no. 1, pp. 1–24, 2015.
- [49] T. Inoue, Y. Kitamura, Y. Li, and W. Ito, "Robust airway extraction based on machine learning and minimum spanning tree," in *Medical Imaging 2013: Computer-Aided Diagnosis*, vol. 8670. International Society for Optics and Photonics, 2013, p. 86700L.
- [50] F. Milletari, N. Navab, and S.-A. Ahmadi, "V-net: Fully convolutional neural networks for volumetric medical image segmentation," in *2016 fourth international conference on 3D vision (3DV)*. IEEE, 2016, pp. 565–571.
- [51] T.-C. Lee, R. L. Kashyap, and C.-N. Chu, "Building skeleton models via 3-d medial surface axis thinning algorithms," *CVGIP: graphical models and image processing*, vol. 56, no. 6, pp. 462–478, 1994.

- [52] H. He and E. A. Garcia, "Learning from imbalanced data," *IEEE Transactions on knowledge and data engineering*, vol. 21, no. 9, pp. 1263–1284, 2009.
- [53] C. Wei, K. Shen, Y. Chen, and T. Ma, "Theoretical analysis of self-training with deep networks on unlabeled data," *arXiv preprint arXiv:2010.03622*, 2020.
- [54] S. G. Armato III, G. McLennan, L. Bidaut, M. F. McNitt-Gray, C. R. Meyer, A. P. Reeves, B. Zhao, D. R. Aberle, C. I. Henschke, E. A. Hoffman *et al.*, "The lung image database consortium (lidc) and image database resource initiative (idri): a completed reference database of lung nodules on ct scans," *Medical physics*, vol. 38, no. 2, pp. 915–931, 2011.
- [55] Y. Xue, H. Tang, Z. Qiao, G. Gong, Y. Yin, Z. Qian, C. Huang, W. Fan, and X. Huang, "Shape-aware organ segmentation by predicting signed distance maps," in *Proceedings of the AAAI Conference on Artificial Intelligence*, vol. 34, no. 07, 2020, pp. 12 565–12 572.
- [56] Z. Xu, U. Bagci, B. Foster, A. Mansoor, J. K. Udupa, and D. J. Mollura, "A hybrid method for airway segmentation and automated measurement of bronchial wall thickness on ct," *Medical image analysis*, vol. 24, no. 1, pp. 1–17, 2015.
- [57] M. Zhang, G.-Z. Yang, and Y. Gu, "Differentiable topology-preserved distance transform for pulmonary airway segmentation," *arXiv preprint arXiv:2209.08355*, 2022.
- [58] E. Smistad, A. C. Elster, and F. Lindseth, "Gpu accelerated segmentation and centerline extraction of tubular structures from medical images," *International journal of computer assisted radiology and surgery*, vol. 9, no. 4, pp. 561–575, 2014.
- [59] A. Paszke, S. Gross, F. Massa, A. Lerer, J. Bradbury, G. Chanan, T. Killeen, Z. Lin, N. Gimelshein, L. Antiga *et al.*, "Pytorch: An imperative style, high-performance deep learning library," *Advances in neural information processing systems*, vol. 32, 2019.
- [60] F. Pérez-García, R. Sparks, and S. Ourselin, "Torchio: a python library for efficient loading, preprocessing, augmentation and patch-based sampling of medical images in deep learning," *Computer Methods and Programs in Biomedicine*, p. 106236, 2021.
- [61] H. Chen, Q. Dou, L. Yu, J. Qin, and P.-A. Heng, "Voxresnet: Deep voxelwise residual networks for brain segmentation from 3d mr images," *NeuroImage*, vol. 170, pp. 446–455, 2018.